

Citation for published version:

M. A. Attar, H. Zhao, M. R. Herfatmanesh, and A. Cairns,
“Turbulent flame boundary and structure detection in an
optical DISI engine using tracer-based two-line PLIF technique”,
Experimental Thermal and Fluid Science, Vol. 68: 545-558,
November 2015.

DOI:

<https://doi.org/10.1016/j.expthermflusci.2015.06.015>

Document Version:

This is the Accepted Manuscript version.

The version in the University of Hertfordshire Research Archive
may differ from the final published version. **Users should
always cite the published version of record.**

Copyright and Reuse:

© 2015 Elsevier Inc. All rights reserved.

This Manuscript version is distributed under the terms of the
Creative Commons Attribution licence

<https://creativecommons.org/licenses/by-nc-nd/3.0/>.

Enquiries

If you believe this document infringes copyright, please contact the
Research & Scholarly Communications Team at rsc@herts.ac.uk

Turbulent flame boundary and structure detection in an optical DISI engine using tracer-based two-line PLIF technique

Mohammadreza Anbari Attar*, Hua Zhao, Mohammad Reza Herfatmanesh, Alasdair Cairns

Centre for Advanced Powertrain and Fuels Research, Brunel University London, UK

Abstract

Design and development of new combustion systems for Spark Ignition Direct Injection (DISI) engines requires thorough understanding of the combustion flame as it develops from the electric discharge and propagates across the combustion chamber. The main purpose of this work was to develop an experimental setup capable of investigating the premix turbulent flame boundary and structure inside the combustion chamber of a DISI engine. For this purpose the tracer-based two-line Planar Laser Induced Fluorescence (PLIF) technique was set up. In order to have a thermometry technique independent of the photophysical model of dopant tracer, a specially designed Constant Volume Chamber (CVC) was utilized for quasi in situ calibration measurement. The thermometry technique was evaluated by measurements of average in-cylinder charge temperature during compression stroke for both motoring and firing cycles and comparing the results with temperature values calculated from in-cylinder pressure data. The developed technique was successfully implemented to detect flame structure during combustion process in an optical engine. The present study demonstrated that as the two-line PLIF thermal images are independent of species concentration and flame luminosity they can be utilized as an accurate means for flame segmentation. The proposed technique has the potential to be utilized for study of premix flames in non-homogeneously mixed systems.

Keywords: Planar Laser Induced Fluorescence (PLIF); Thermometry; Flame boundary and structure; Premixed/partially-premixed turbulent flame;

Nomenclature

Roman symbols	V Volume
A flame surface area	X_{tr} tracer mole fraction
c speed of light	Greek symbols
c_p specific heat at constant pressure	δ flame front thickness
E laser fluence	η_c transmission efficiency of optics
h Planck constant	λ excitation wavelength
k flame stretch rate	σ absorption cross section
m mass	ν spatial frequency
M molecular weight	ϕ fluorescence Quantum Yield (FQY)
n polytropic constant	Ω_c collection solid angle of optics
L latent heat of vaporization	Superscript
P pressure	AVG averaged image
Q energy	SIG single image
\tilde{R} specific gas constant	
S number of photons incident per pixel	
T temperature	

1. Introduction

Performance, efficiency and emissions of Internal Combustion (IC) engines are governed by flame and combustion process. For the spark ignition engine the flame initiation and propagation are of primary concern as both alter the burn rate which directly affects the thermal efficiency and cycle to cycle variation [1]. The flame quenching has also been considered as one of the main mechanisms contributing to the emission of hydrocarbons. It has been shown that under lean, low-load or high EGR conditions, the operating range of SI engines is limited by the level of cycle-by-cycle variation as a result of variation in flame formation and development [2, 3]. Therefore thorough understanding of the combustion phenomena involving ignition, flame formation, propagation and extinction can significantly contribute to the improved engine design, in terms of performance, efficiency and emissions control.

In spark ignition gasoline engines the injected fuel droplets quickly evaporate and mix with the inlet air to form a combustible mixture. The mixture is then ignited e.g. by an electric discharge from a spark plug and initiate a kernel. The flame is developed from this kernel, propagates across the cylinder and extinguishes at the cylinder wall. In such flames, chemical kinetics and flow of heat and mass play equally important roles. In the early stages, kernel formation is susceptible to the initial mixture preparation, ignition source and in-cylinder charge flow motion. While after the kernel developed, its growth is mainly determined by the chemical and physical properties of the mixture and the geometry of the combustion chamber [4]. Therefore in conventional Port Fuel Injection (PFI) spark ignition engines, the flame can be classified as a premixed (fuel and oxidizer are uniformly mixed together prior to the ignition), turbulent (due to the in-cylinder charge turbulent flow through the flame) and unsteady (as the flame structure and motion change with time) [4B]. However for the Direct Injection Spark Ignition (DISI) engines, under certain operating conditions we encounter partially-premixed flames as well as diffusion flames. For the diffusion flame, the fuel ignites in a liquid phase (rather than in a gas phase) as the reactants mix together through a diffusion process in the same region where the reaction takes place. The diffusion flame in DISI engines occurs due to retarded injection timings or as a result of fuel impingement on the piston or cylinder liner. Subsequently, investigation of the combustion flame in DISI engines especially under stratified condition is more challenging compared to the PFI engines. For analysis of turbulent flames, Karlovitz et al. [5] introduced the concept of flame stretch. Williams [6] suggested the definition of stretch rate as the temporal rate of change of flame area per unit area:

$$\kappa = \frac{1}{A} \frac{dA}{dt} \quad (1)$$

This concept has been widely used to investigate flame propagation in the IC engines. However as it can be seen, the flame stretch calculation relies on the measurement of the flame surface area which intern depends on how accurately we can define the flame front position. In addition to the flame stretch measurements, the flame front thickness can be used for a rough estimation of the temperature of the combustion products using

$$\delta \cong \frac{T_p - T_r}{(dT/dx)_{max}} \quad (2)$$

where δ is the flame front thickness, T_p and T_r are the temperature of the combustion products and the reactants respectively and dT/dx is the maximum temperature gradient which occurs at the point of inflexion of the profile [4].

Several different techniques have been suggested and applied for the flame investigation in the course of the last few decades. Such techniques either track photons or particles from the combustion. The most common imaging techniques include direct photography, shadowgraph, Schlieren, interferograph, Mie scattering, and single-line PLIF. In the case of direct photographic techniques, the flame luminosity is directly captured by a camera or optical fibres (e.g., [7, 8]). The burned luminous zone is defined as the region behind the flame front. The flame front itself consists of two regions: a preheat zone and a reaction zone [9]. In the preheat zone the temperature of the unburnt mixture increases to the ignition point. From this point the exothermic chemical reactions start in the reaction zone and temperature rises exponentially and reaches to the adiabatic flame temperature just past the luminous zone. As the flame luminosity is mostly not high enough for the direct photography, an image intensifier is coupled with the camera to increase the Signal to Noise Ratio (SNR) which in turn reduces the spatial resolution. In a work carried out by Zeng et al., they have significantly increased the flame luminosity by addition of sodium-containing additive to the gasoline, enabling high speed imaging at 12k Hz without an intensifier [10]. However the other deficiency of the direct photographic techniques is the fact that as the luminous zone is mainly produced by hot incandescent products of combustion, the flame surface recorded by this technique is the 'post flame' region rather than the actual flame front. Interferograph, shadowgraph and Schlieren techniques exploit the deflection of light due to variation of the refractive index as a result of density non-uniformities in the enflamed area. The interferograph (e.g., [11]) gives an indication of the density field or temperature itself and it is only applicable to two-dimensional flames. Shadowgraph indicates the field of second derivative of density. Assuming that the density field across the flame is a consequence of the temperature variation ($\rho \propto 1/T$), the technique measures $\partial[(-1/T^2)(\partial T/\partial x)]/\partial x$. The Schlieren technique on the other hand indicates the field of density gradient $(-1/T^2)(\partial T/\partial x)$, this surface is more definable than shadowgraph surface and is closest to the fresh mixture and therefore more suitable than the other two techniques for the measurements of the enflamed area [12, 13].

Planar laser Mie scattering techniques of smoke or seeded particles [14- 16], single-line PLIF of different combustion species and dopants [17- 24] have been employed to study the flame structure and its growth. However neither of these techniques can precisely detect the flame edge and the flame structure in DISI engines as they are all dependent on the dopant/species concentration. This is due to the fact that delivery of the fuel directly into the cylinder inherently results in a delay in charge mixing compared to the port fuel injection. Ultimately, some degree of charge stratification often remains, even under “homogeneous” targeted conditions [25, 26].

In addition to the above mentioned common techniques, there are a number of techniques which have been utilized for flame study since late 70s' [27, 28]. In particular, applications of Raman and Rayleigh scattering techniques have been investigated extensively. However, despite the significant improvements in measurements [e.g., 29- 33], these techniques are still not suitable for engine applications. While Raman scattering is inelastic scattering similar to the fluorescence, Rayleigh scattering is an elastic process, so that the scattered signal occurs at the same wavelength as the excitation source. For this reason, the Rayleigh signal is subject to interference from the intense scattered light produced by particles and nearby surfaces. Also being an elastic process, Rayleigh scattering is not species specific and requires measurements of local species concentration. However, the main issue is that for the same experimental conditions, the relative signal power for each scattering method depends primarily on the differential cross section; and that the differential cross section of the Raman and the Rayleigh scattering are orders of magnitude smaller than the fluorescence and the Mie scattering [34]. Because of their low differential cross sections, Raman and Rayleigh scattering measurements normally require high species concentrations. Among these four scattering methods, in addition to Mie, only fluorescence offers the intensity and spectral selectivity for measurements in moderately dirty flows, where interferences can also arise owing to blackbody radiation, flame emission, or laser-induced incandescence.

The trace-based Planar Laser Induced Fluorescence (PLIF) is a well-known versatile and powerful diagnostic technique for flow and combustion measurements. It has been utilized for spray imaging, study of charge stratification and measurements of local air-fuel ratio, charge temperature and Exhaust Gas Residuals (EGR). In this work isoctane was used as a surrogate fuel due to its similar physical and thermodynamic properties to typical gasoline fuels and 3-pentanone was chosen as a seeding tracer. The main physical and photophysical properties required of a fluorescent tracer for in-cylinder LIF studies include: boiling point and transport properties closely match to the carrier fuel, absorption spectrum suitable for available laser wavelengths, satisfactory fluorescence quantum yield, and insensitivity to oxygen quenching [35]. Previous studies of the photophysical behaviour of 3-pentanone indicated its advantages over other common tracers [36-39]. Grossmann et al. studied the temperature and pressure dependence of the LIF signal of gas-phase 3-pentanone and showed that after excitation at two different wavelengths the ratio of the fluorescence signal intensities reflects the local temperature. Since this temperature measurement is based on the ratio of signal intensities it is independent of local tracer concentrations and therefore allows measurements of two-dimensional temperature distributions in non-homogeneously mixed systems [40]. Einecke et al. [41] reported the first application of the two-line PLIF technique for temperature distribution measurements in an optically accessible two-stroke engine with isoctane doped with 3-pentanone. Rothamer et al. have proposed the combination of 308 nm and 277 nm excitation wavelengths for simultaneous measurements of temperature and EGR of a Homogenous Charge Compression Ignition (HCCI) engine [42]. This work has been followed in similar researches to study the Negative Valve Overlap (NVO) strategy in HCCI operation [43]. However in these latter works, in-cylinder charge temperature values were calculated using theoretical models of 3-pentanone and estimated temperatures based on isentropic compression and 1-D engine simulation were used as reference data to modify parameters of the photophysical model and tune it to give the most accurate temperature readings on particular test conditions. In this work the two-line PLIF technique was setup and optimized for charge temperature measurements independent of the tracer's model by means of in situ calibration utilizing a specially designed Constant Volume Chamber (CVC). The current paper presents a method to extend the two-line PLIF applications for the flame boundary and structure detection. As each of the flame preheat reaction and luminous zones are at a specific temperature range, the proposed two-line PLIF thermal images enable precise detection of the flame structure independent of species concentration or flame luminosity.

2. Principle of the two-line PLIF thermometry

Fluorescence is considered as the sequence of an optical absorption process followed by a spontaneous emission event. The precise definition of fluorescence requires that emission occurs between electronic energy states of the same multiplicity, i.e., same electronic spin states. Emission between states of different electronic spin is termed phosphorescence. In the linear regime, the laser induced fluorescence signal is given by

$$S_f = \frac{E}{h\nu} \left[\frac{V_e X_{tr} P}{kT} \right] \sigma(\lambda, T) \phi(\lambda, T, P, X_{tr}) \frac{\Omega_c}{4\pi} \eta_c \quad (3)$$

where S_f is the number of photons incident per pixel at the detector or the photocathode of an intensified camera [photons/pixel], E is the laser fluence [J/cm^2], ν is the spatial frequency of the incident laser radiation [cm^{-1}], V_e is the excited volume [cm^3], X_{tr} is the tracer mole fraction, P is the total pressure [MPa], T is the temperature [K], σ is the absorption cross

section [cm²], ϕ is the fluorescence quantum yield (FQY), Ω_c is the collection solid angle of the optics used for imaging the fluorescence, and η_c is the transmission efficiency of optics and filters used in the imaging setup. Both the absorption cross section and FQY vary by temperature while the rate of these variations depends on the excitation wavelengths. In order to determine temperature, an absorption specie should be chosen so that its fluorescence signal ratio for two given excitation wavelengths exhibits strong temperature dependence. For 3-pentanone, the absorption band extends from 220 to 340 nm with a peak near 280 nm at the room temperature. As the temperature increases, the peak intensity red-shifts so e.g. at 1000 K, the peak occurs at \sim 290 nm [40]. This spectral shift of the absorption spectra can be used for temperature measurements by choosing two excitation wavelengths on different wings of this band and taking the ratio of fluorescence signals from these two excitation wavelengths. The 3-pentanone fluorescence signal is emitted between 350 and 550 nm with a maximum at 420 nm. When fluorescence signals from two excitation wavelengths are detected, their ratio is given by

$$\frac{S_{f2}}{S_{f1}} = \frac{E_2 v_1}{E_1 v_2} \times \frac{\sigma_2}{\sigma_1} \times \frac{\phi_2}{\phi_1} \quad (4)$$

In the two-line PLIF thermometry, high-energy pulsed lasers are employed to generate two laser pulses at required wavelengths with a very short time delay. The laser pulses are formed into thin (sub millimeter) laser sheets and steered to the sampling area inside the engine by the transmitting optics. The fluorescence signals from both excitations are captured and amplified by an ICCD camera. The time delay between camera gates is typically kept as short as few microseconds. This is to ensure that the images are taken at a frozen condition with a minimum change in thermodynamic state of the measurement volume between two images.

3. Experimental setup

3.1. Test Engine

A single cylinder optical DISI engine, shown in Figure 1, was used for the experiments. The engine employed a prototype DI head featuring a pent-roof combustion chamber with four valves operated by double overhead camshafts. Table 1 summarizes the engine specification. Optical access to the engine was achieved by modifying the cylinder block so it allowed a sandwich plate to be installed between the cylinder block and cylinder head. The sandwich plate housed four windows on its sides which could be used for illumination or side imaging of the combustion chamber. A quartz window was installed in the piston crown and a 45° mirror mounted on the cylinder block provided the bottom view of the combustion chamber. A direct injector (DI) and a Port Fuel Injector (PFI) were employed to inject the fuel (isooctane) into the combustion chamber and the tracer (3-pentanone) into the intake port respectively.

Table 1 Key engine specifications

Combustion chamber	Pent-roof
Displaced volume	450 cc
Bore	80 mm
Stroke	89 mm
Inlet valves diameters	29.5 mm
Exhaust valves diameters	21 mm
Valve lift	4 mm
Valve duration	110 °CA
Compression Ratio	12.4:1

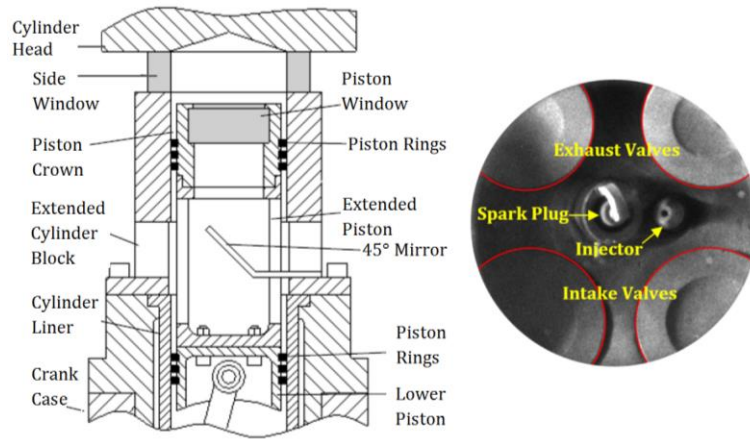


Fig. 1 Left: Single cylinder gasoline direct injection engine, Right: spray guided combustion chamber

3.2. Two-line PLIF setup

3.2.1 Excitation wavelengths

Two excitation wavelengths at 308 nm and 277 nm were used for the measurements. The 308 nm pulses were obtained from a Xenon Chloride (XeCl) laser (Lambda Physik COMPexPro 102) output while the 277 nm pulses were generated by Raman shifting a Krypton Fluoride (KrF) laser output (Coherent COMPex 102) at 248 nm to 1st Stoke of H₂ using a bespoke Raman Converter (RC). As the KrF laser output beam was 10 mm × 24 mm (horizontal × vertical), and in order to avoid using extra lenses (a reverse Galilean telescope) to resize the laser beam, the RC was designed with an aperture size of 25.4 mm and two Lithosil lenses with anti-reflection coating at 248 nm to 277 nm and thickness of 15.8 mm were used as the converter's input and output windows to focus the laser beam into the RC and re-collimate the output. A series of tests were carried out on the RC to find the maximum conversion efficiency with the minimum pulse to pulse variation as a function of RC fill pressure and input pulse energy. Based on the experimental results in [44], the RC was filled with grade 5 hydrogen (purity 99.999%) at 55 bar (800 psi) to provide the maximum conversion efficiency with the lowest output pulse energy fluctuation. Also to achieve the maximum pulse energy with the lowest fluctuation, Excimer lasers were operated with fresh gases. This was done by purging lasers' resonator and refilling it with fresh premix gas prior to each test. Also both lasers were run at constant energy mode. In this mode, lasers' internal energy meter monitor the output pulse energy and vary the resonator high voltage to keep the output pulse energy constant. Thus, lasers could provide output pulses with a very low energy fluctuation (<1.8% and <0.8% standard deviation for XeCl and KrF lasers respectively). Furthermore, pulse energy variations of both lasers were monitored and recorded prior to each test to make sure they were in an acceptable range.

3.2.2 Beam Delivery and Shaping System

In order to reshape the lasers output and produce two thin, spatially overlapped laser sheets at the measurement plane inside the combustion chamber, an optical system was designed and arranged on two anti-vibration optical tables. While the upper table had a fixed height relative to the engine, the lower table utilized levelling fits that allowed alignment of the table height with the Excimer lasers' output. Figure 2 shows the schematic diagram of the two-line PLIF system. A beam splitter (10×10 cm²) was placed right after the XeCl laser to reduce the output pulse energy. Although the maximum pulse energy of the XeCl laser at 308nm (200 mJ) was less than the KrF laser at 248 nm (400 mJ), due to a low Raman conversion efficiency and the fact that it was not possible to run the KrF laser continuously at its peak pulse energy, the maximum pulse energy of the RC output at 277 nm available at the measurement area was less than 30 mJ. One solution was to run the XeCl at lower pulse energy but it was found that, this results in a very high pulse to pulse energy fluctuation. Therefore the XeCl laser was run at high output pulse energy and the beam splitter was used to reduce the energy to minimize the pulse to pulse variation of the 308 nm laser sheet. The beam splitter was coated for the 50% transmission of 308 nm beam at 45° incident angle and it was possible to alter the transmission by rotating the beam splitter. An equatorial dispersive prism with Anti Reflection (AR) coating at 277 nm was placed after the RC so that the higher Stokes and anti-Stokes can be separated from the desired wavelength. Four High Reflective (HR) mirrors at 308 nm and three HR mirrors at 277 nm were used for steering the beams into the combustion chamber. It should be noted that a minimum of three mirrors were required to raise and flip the beams at each wavelength. The main reason for flipping the beams was the fact the laser beams' divergence on the vertical axis of the laser output was much higher than on the horizontal axis. By flipping the laser beams, laser sheets in the measurement area would exhibit little divergence in their thickness as they expanded horizontally. To overlap the two excitation beams a Dichroic Mirror (DM) was used. The dichroic mirror had same dimensions as the other HR mirrors but with special coating that transmitted one laser beam at 308 nm with >90%

efficiency while reflected the other wavelength at 277 nm with >97% efficiency. A rectangular cylindrical lens 76.2×38.1 mm² with focal length of 1500 mm and a broad band AR coating was used to turn the expanded laser beams to laser sheets. The coating provided both a very low reflection of ≤0.5% over a broad UV range from 248 nm to 355 nm and high damage threshold of 10 J/cm² (at 1064 nm, 20 ns FWHM and 20 Hz).

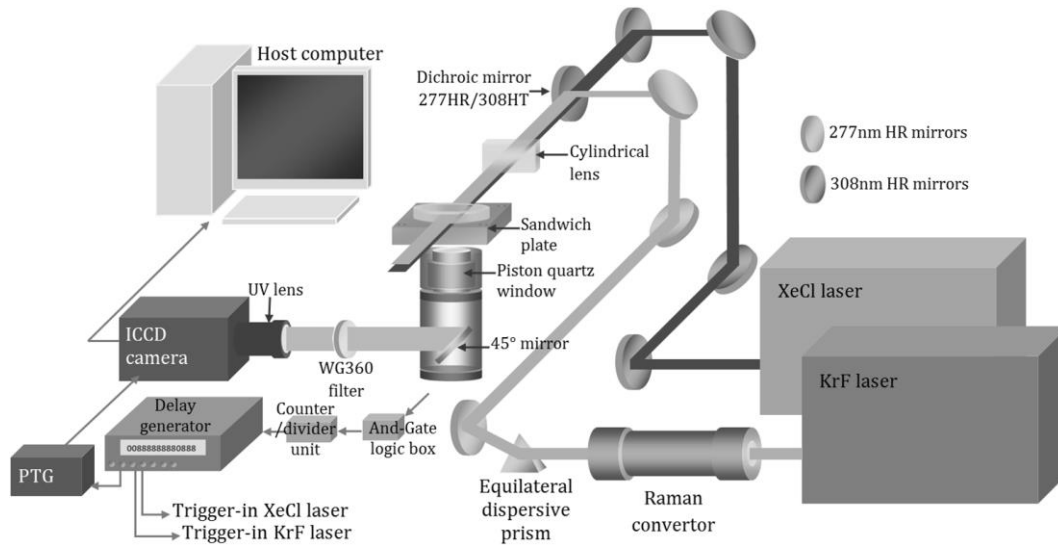


Fig. 2 Schematic diagram of the two-line PLIF setup

3.3.3 Imaging System

The image acquisition in this research was carried out with a Princeton Instrument PI-MAX II intensified CCD camera system. The system components were the camera head (houses the CCD, intensifier and a multi-stage Peltier cooler), ST-133 controller with the Programmable Timing Generator (PTG), a host computer with an interference card and Princeton Instrument WinView/32 software. For the two-line PLIF imaging, the overlapped read out mode was exploited. The overlapped operation allowed a new exposure to begin while the readout of the previous one is still in progress, enabling the camera to capture two images with an extremely short interval. A UV-Nikkor 105 mm f/4.5 macro photography lens was coupled with the camera and a Schott WG360 long pass filter was used to block the unwanted wavelengths. Several different techniques were employed to enhance the fluorescence SNR and imaging quality. Light reflections from the combustion chambers' roof and cylinder walls were reduced by covering the cylinder head with candle soot and focusing laser sheets behind the sandwich plate. Rayleigh and Mie scattering signals were significantly reduced by using an appropriate long pass filter, fine adjustment of the ICCD gate timing, and exploiting extra short gate widths. The fine adjustment of the ICCD gating was achieved by a precise time budgeting through study of all the delays in electronic devices. The CCD accumulated dark charge was minimised by operating the camera at the lowest CCD array temperature for the test conditions (-20 °C) as well as programming the camera to perform CCD clean cycles while the intensifier was waiting for start acquisition command. Furthermore, the background subtraction was performed during the image post-processing to further enhance the SNR.

3.3.4 Engine-PLIF system synchronization

For the synchronization, the engine reference signal which had 10 Hz frequency at engine speed of 1200 rpm was used to trigger the illumination and light capturing systems. The Excimer lasers maximum repetition rate was also 10 Hz and therefore this signal could be used to trigger the lasers. But the camera readout frequency at full CCD (1024×1024 pixels) was 4 Hz. Therefore to be able to use the 10 Hz trigger-in signal for the imaging system, either a Region of Interest (ROI) should be assigned on the camera CCD or the imaging pixels binned together (at 2×2 to 16×16). The ROI may be the entire CCD array (full chip) or it may be a rectangular sub-region of the array. However the actual size of the measurement area on the CCD is dictated by the optical lens aperture size and its focal length, and setting a smaller ROI results in shrinking the actual measurement area. On the other hand in the binning process, the data from adjacent pixels (vertically or horizontally) are added up together to form a single (super) pixel. On the PI camera binning could be set up to occur during data acquisition (hardware binning) or after the data has been sent to the host computer (software binning). The hardware binning improves the SNR and as it is performed before the signal is read out by the preamplifier, the readout time and the load on computer memory are reduced. However this sacrifices the resolution and may results in pixel saturation and blooming. In this case the software binning can be exploited but this binning process is not as fast as the hardware binning and does not improve the SNR while decreasing the resolution. In the present work, an alternative technique based on an external Counter/Divider unit was deployed. The Counter/Divider unit receives the 10 Hz engine

reference signal and provides a trigger-in signal at lower frequencies. This signal can be used for the PLIF system as well as injection system (for skip injection operation where the fuel injection takes place only at the required cycles). The output of the Counter/Divider board was sent to a delay generator to trigger both the lasers and the camera while the camera PTG was utilized for fine adjustment of the ICCD gate width and delay. Figure 3 shows the timing diagram of the two-line PLIF diagnostic. 'd₁' is the delay between engine reference signal (T₀) and the delay generator output for both the XeCl laser (T_A) and the ICCD camera (T_C). This delay (T₀ to T_A and T_C) was used for imaging at different engine crank angles. 'd₂' delay at the XeCl laser, 'd₃' delay between XeCl and KrF laser trigger-in signals, 'd₄' delay at KrF laser and 'd₅' is gate delay at the camera PTG.

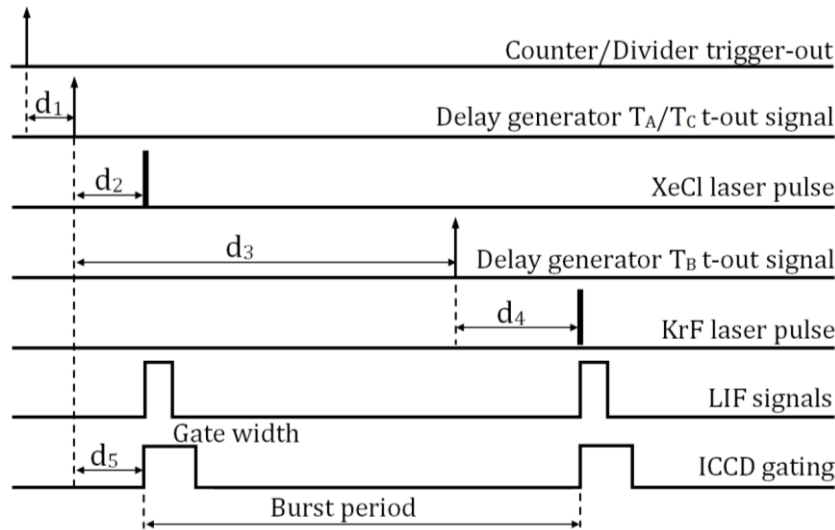


Fig. 3 Timing diagram for capturing a DIF

4. Temperature calibration measurements

In order to perform quasi in situ calibration measurements, a constant volume chamber (CVC) was designed and manufactured so it can be mounted on the engine block in place of cylinder head (as it is shown in Figure 4). Same optical components (side windows and piston window) were utilised on both the CVC and the engine. This was to eliminate any effect of variation in light transmission efficiency and surface flatness of different optics. To supply the tracer into the CVC, a metal tank was filled with liquid 3-pentanone, cartridge heaters were used to heat up (to 318 K) the tracer inside the tank and a nitrogen bottle was connected to the bottom of this tank through a second regulator. By setting the bath gas pressure and adjusting the inlet and outlet valve openings on the chamber, continuous flow of homogenous mixture of the tracer and the bath gas was introduced into the chamber. A combination of tubular heaters (wrapped around the CVC) and cartridge heaters (placed inside the CVC liner) were used to heat up the premixed charge and achieve high gas temperatures in combination with short residence times to avoid decomposition of the tracer. Three NiCr-Ni thermocouples (with response time of 0.25 s at 300 K and 0.5 s at 800 K), two in contact with the CVC wall and one placed at the centre of CVC cavity and isolated from the CVC body, were used to monitor chamber wall and charge temperature respectively.

For the PLIF measurements, camera mode was set to Double Image Frame (DIF) with a gate width and burst period of 1 μ s and 5 μ s respectively and a shutter compensation time of 4 μ s. This time was the amount of time inserted between the end of exposure time and the beginning of the array readout which allowed time for phosphor to decay (the lowest residual intensity on the second image for different burst periods was observed when the shutter compensation time was close to the burst period). To obtain temperature calibration curve, a set of 20 background DIFs (20 images at 277 nm excitation and 20 images at 308 nm excitation) was captured prior to seeding the chamber at the room temperature. Then the CVC and tracer tank heating systems were switched on and a set of 20 data DIFs was captured at each selected temperature up to 750 K at 2 bar chamber pressure. Using an image processing code each set of DIFs was first divided into two stacks of even images ('E', laser illumination at 277 nm) and odd images ('O', laser illumination at 308 nm). Then average of each data stack was calculated and subtracted by its averaged background image. In order to eliminate the effect of boundary layers, a region of interest (ROI), 600 \times 600 pixels (40 \times 40 mm²), located at the centre of the CVC cavity (shown in Figure 5a), was defined on the resultant images and the pixels' value within the ROI were averaged. Finally the ratio of two fluorescence signals was calculated. Figure 6 shows the result. The diamond and cross markers represent fluorescence signal intensity as a function of CVC temperature for laser illumination at 308 nm (I_O) and 277 nm (I_E) respectively. The calibration curve, solid black

line, was obtained by fitting a linear trend line on the calculated fluorescence signal ratio, $R (I_o/I_E)$, at different chamber temperature.

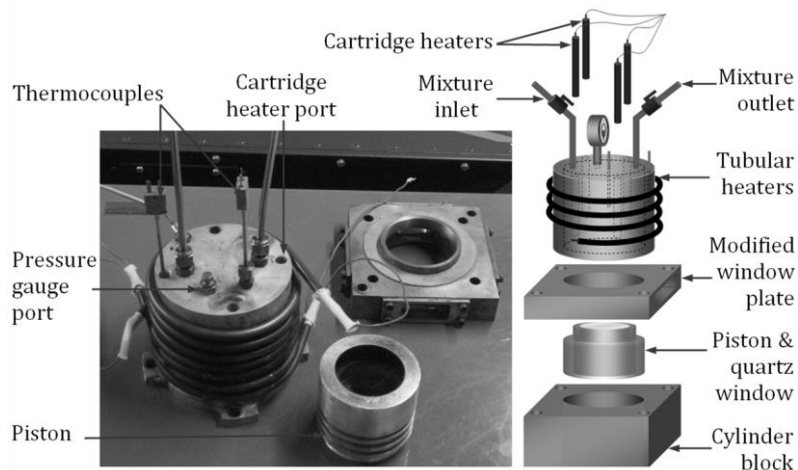


Fig. 4 Constant volume chamber components

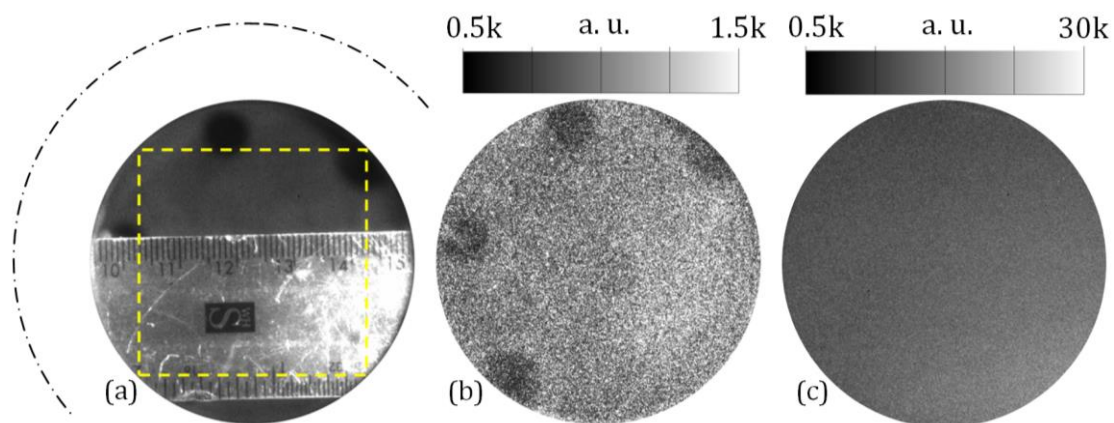


Fig. 5. (a) Imaging lens was focused on the measurement plane inside the CVC, dashed square and dashed-dotted circle indicate the ROI and inner diameter of the chamber respectively (b) single-shot background image, (c) single-shot data image

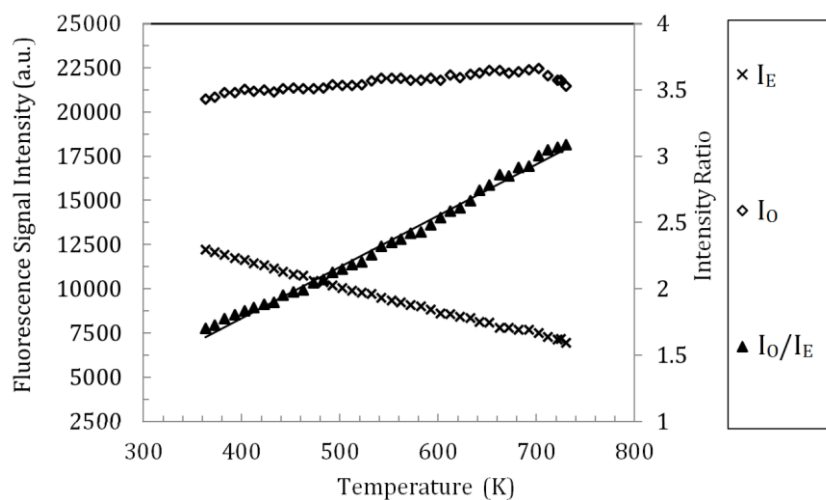


Fig. 6. Fluorescence signal intensities of two excitation wavelengths and the PLIF temperature calibration curve

It was observed that while the fluorescence signal intensity for the excitation at 277 nm drops as the temperature increases, the fluorescence signal intensity for the excitation at 308 nm slightly increases and the ratio of two signals showed a linear increase. The absolute value of the coefficient of variation (COV) of the temperature calibration measurements was less than 3%. This was calculated by comparing 20 single DIFs at each selected temperature. This uncertainty was partially due to inaccuracy of ± 0.25 K in CVC charge temperature control during measurement at each point. In addition, the relative standard deviation of the averaged signal intensity of the ROIs was found to be $\sim 1.9\%$ and $\sim 1\%$ for excitation at 308 nm and 277 nm respectively. Both these values were close to the relative standard deviation of the lasers' pulse energy fluctuation, indicating that the actual precision of the single-shot thermometry technique could be further enhanced by correcting for the pulse energy fluctuation of lasers. However as the single-shot thermometry technique was not the focus of this work and temperature values were calculated from averaged DIFs, application of this correction was not beneficial. The choice of nitrogen as the bath gas (instead of air) for calibration measurements was due the fact that the two-line PLIF system was initially designed to be implemented for Controlled Auto Ignition (CAI) combustion measurements with $\sim 60\%$ exhaust gas internal recirculation. Although the ideal condition for the calibration measurements would be a case of having exactly the same charge composition as the engine measurements, but previous studies indicated that the ketones' fluorescence at atmospheric pressure is relatively insensitive to the bath gas composition and quenching due to the dominant non-collision dependent decay rates of the first excited singlet state [45, 46]. In addition, experimental test results at elevated pressures up to 20 bar, indicated that 3-pentanone shows even less sensitivity to oxygen-related quenching influences than does other ketones [47] which was associated with the electron density at the carbonyl group [48]. In addition, it should be noted that although the temperature calibration measurements did not cover the full range of in-cylinder charge temperature values for spark ignition engine operation, but it was sufficient for global charge temperature measurements during the compression stroke and up to ignition timing as well as local end-gas temperature measurements during the combustion.

4.1 Measurements of in-cylinder charge temperature

The two-line PLIF experimental setup for in-cylinder charge temperature measurements was identical to the calibration measurements. Isooctane was introduced by direct injection into the combustion chamber using an air-assisted low pressure direct injector while the tracer was injected (mole fraction of 0.4% in total charge) into the intake port via a port fuel injector to achieve a homogenous tracer seeding. Intake port was insulated with heat resistant fiberglass tape and the intake air was heated to 318 K to facilitate the tracer vaporization. In order to ensure stable thermal conditions, engine was warmed up prior to the measurements with both engine oil and coolant temperatures fixed at 363 K and 313 K (± 2 K) respectively. Three sets of 40 DIFs were captured at desired crank angles from 94 °CA BTDC to 35 °CA BTDC (ignition timing) during the compression stroke at the engine speed of 1200 rpm. The first set was background frames (BK) with both lasers on and both port and direct injectors off. The second set was motoring frames (PFI) in which both lasers and PFI injector were on but the DI injector was switched off. Finally the third set was firing frames (DI) in which both lasers and both injectors were switched on. To minimize effects of windows fouling on the measurements, all the three sets of frames at each crank angle were captured following each other. In-cylinder charge temperature for motoring and firing cycles were measured by first calculating fluorescence signal ratios using:

$$R_{motoring} = \frac{PFI(O)_{X^{\circ}CAD}^{AVG} - BK(O)_{X^{\circ}CAD}^{AVG}}{PFI(E)_{X^{\circ}CAD}^{AVG} - BK(E)_{X^{\circ}CAD}^{AVG}} \times \frac{PFI(E)_{94^{\circ}CA BTDC}^{AVG} - BK(E)_{94^{\circ}CA BTDC}^{AVG}}{PFI(O)_{94^{\circ}CA BTDC}^{AVG} - BK(O)_{94^{\circ}CA BTDC}^{AVG}} \quad (5)$$

$$R_{firing} = \frac{DI(O)_{X^{\circ}CAD}^{AVG} - BK(O)_{X^{\circ}CAD}^{AVG}}{DI(E)_{X^{\circ}CAD}^{AVG} - BK(E)_{X^{\circ}CAD}^{AVG}} \times \frac{PFI(E)_{94^{\circ}CA BTDC}^{AVG} - BK(E)_{94^{\circ}CA BTDC}^{AVG}}{PFI(O)_{94^{\circ}CA BTDC}^{AVG} - BK(O)_{94^{\circ}CA BTDC}^{AVG}} \quad (6)$$

where R is the normalized fluorescence ratio of the two excitation wavelengths, 308 nm (O image) by 277 nm (E image), and 'AVG' superscript stands for averaged image. Figure 7 shows the image processing steps where the background corrected averaged (of 40 images) motoring and firing image at each crank angle were divided by the background corrected averaged motoring image taken at 94 °CA BTDC in the compression stroke to remove the effects of laser sheet attenuation across the imaging area. Then the calibration curve obtained from constant volume chamber was used to convert the calculated signal ratios to the temperature readings. In-cylinder charge temperature was also calculated from the pressure data to compare with the PLIF temperature measurements. This was done by considering the engine as a closed thermodynamic system between Intake Valve Closure (IVC) to the ignition timing and taking the IVC timing as the reference point for the calculation. During the operation with normal valve timing, fresh charge temperature slightly increases between the Intake Valve Opening (IVO) and the IVC due to heat transfer from the cylinder walls. In the case of the Negative Valve Overlap (NVO)

operation, the charge temperature at IVC is significantly higher than the intake air temperature due to the presence of a large amount of hot residuals. Therefore for the NVO operation, one cannot simply take the intake port temperature as the in-cylinder charge temperature at the IVC. The charge temperature at the start of compression (T_{IVC}) was calculated by the enthalpy balance equation [49];

$$T_{IVC} = \frac{m_s \times c_{p,a} \times T_{in} + m_r c_{p,r} \times T_{ex}}{m_s \times c_{p,a} + m_r \times c_{p,r}} \quad (7)$$

where T_{in} is intake gas temperature measured at 5 cm above the intake port, T_{ex} is exhaust gas temperature measured at 5 cm above the exhaust port, m_s is mass of scavenging charge ($m_s = m_{air} + m_{fuel} + m_{tracer}$) calculated by measuring air flow rate and fuel and tracer injection quantities, m_r is mass of residual gas and $c_{p,a}$ (air) and $c_{p,r}$ (residual gas) are specific heat at constant pressure. The mass of residual gas m_r , is calculated by

$$m_r = \frac{PVM}{\bar{R}T} \quad (8)$$

where P, V, T are at the exhaust valves closure (T from exhaust thermocouple), $\bar{R} = 8.3144 \frac{J}{kg.mol}$ and M is the molecular weight of residual gas. Having calculated the temperature at IVC, the average in-cylinder charge temperature from start of compression to ignition timing was calculated using averaged in-cylinder pressure data (e.g. of 100 cycles) and Equation 7, assuming a polytropic compression

$$T_2 = T_{IVC} \left(\frac{P_{IVC}}{P_2} \right)^{\frac{n-1}{n}} \quad (9)$$

where n is the polytropic constant calculated from $\log P$ - $\log V$ diagram between the IVC to the ignition timing. Figure 8 compares the PLIF temperature values obtained from optical measurements with the values calculated from in-cylinder pressure data. Both techniques showed a very good agreement between two methods with average percent difference of 3% and 2% and standard deviation of 2% and 1% for the motoring and firing cycles respectively. The percent difference at each imaged crank angle was calculated by

$$\text{Percent difference} = \frac{\text{Absolute Difference}}{\text{Average Value}} \times 100 \quad (10)$$

where the *Absolute Difference* was calculated by subtracting temperature value obtained from pressure data by the value obtained from the PLIF images and the *Average Value* was calculated by taking the average of the two temperature values. The standard deviation was then calculated to measure how widely percent difference value at different crank angles were dispersed from the average percent difference.

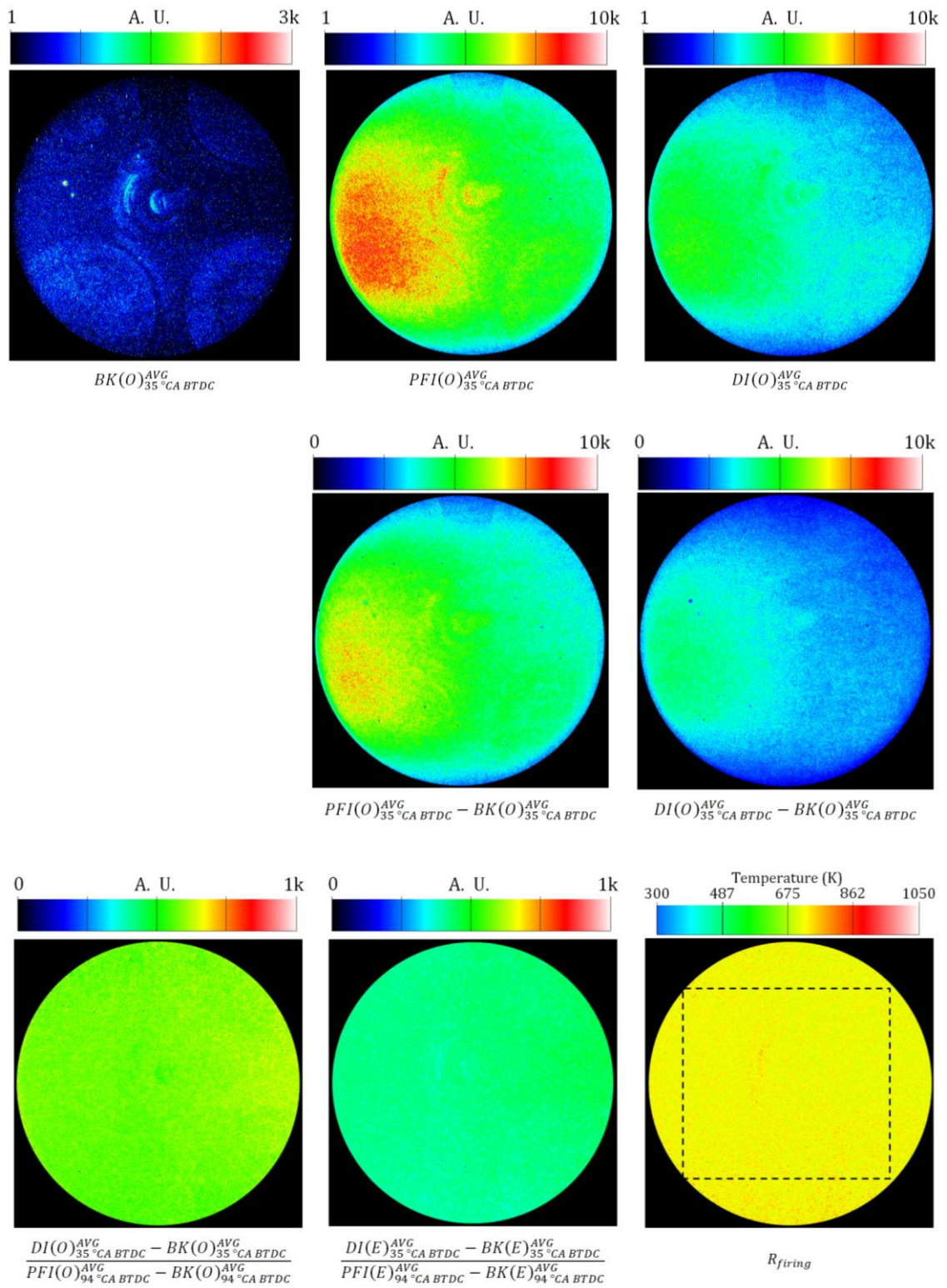


Fig. 7. Two-line PLIF image processing steps for in-cylinder charge temperature measurement

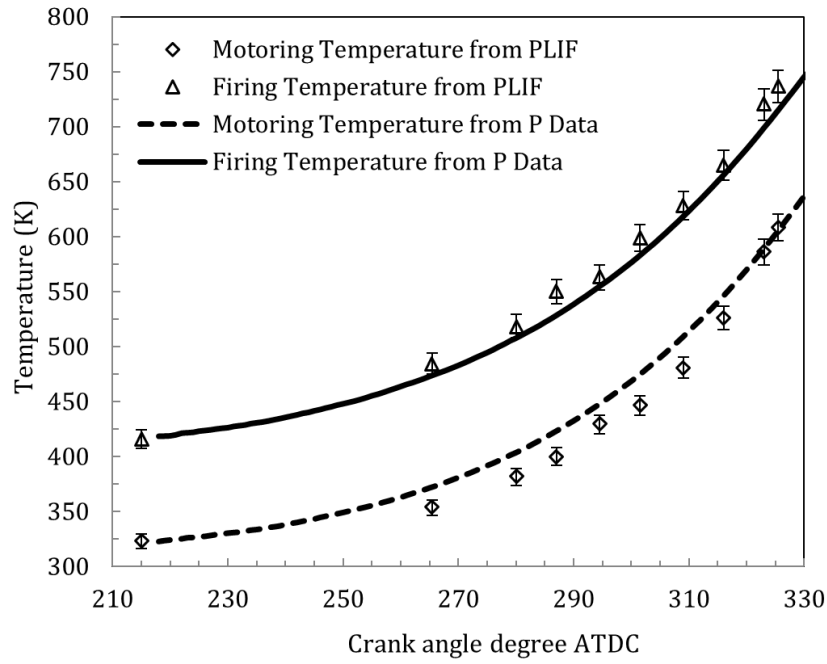


Fig. 8. Averaged in-cylinder motoring and firing charge temperature calculated from both pressure data and two-line PLIF

5. Investigation of premix turbulent flame boundary and structure

5.1 Flame structure detection

In order to extend applications of the two-line PLIF thermometry technique in combustion measurements, we attempted to investigate flame structure and its thermal stratification. There were a number of challenges in applying the tracer-based technique for this study. The first issue was the low fluorescence signal intensity within the enflamed area, as most of the seeded tracer either burn or decompose due to the high gas temperature. However as the 3-pentone two-line PLIF temperature measurement is independent of the tracer mole fraction, by improving the fluorescence SNR, even small quantities of the leftover tracer in the flame region can be utilized for LIF measurements. As the engine piston crown blocked the sandwich plate optical accesses for 25 CAD either side of top dead centre (TDC), it was not possible to illuminate the combustion chamber at the start of flame formation and during early flame development stages with a normal ignition timing. Therefore a series of tests were carried out to find an ignition timing that allows the 2-line PLIF to be carried out while providing a relatively stable engine operation. It was found that ignition timings within 10 CAD either side of TDC result in unstable operation and misfiring in some cycles. The misfiring might be due to failure of the spark plug to generate plasma with enough energy to ignite the charge at the higher in-cylinder pressures and charge density. This can be improved by increasing the coil dwell time and re-gaping the spark plug. While ignition timings around 15 CAD ATDC were found to be a proper choice, later timings resulted in a lower IMEP and much higher COV_{IMEP} . Table 2 summarises the tests results.

Table 2 Engine stability and performance for ignition timing sweep

Ignition Timing	IMEP (bar)	COV_{IMEP} (%)
30 BTDC	5.5	2
20 BTDC	5.3	4
10 BTDC	Unstable operation with some misfiring	
TDC		
10 ATDC		
15 ATDC	4.2	5
20 ATDC	3.3	7

Therefore the ignition timing was retard to 15 CAD ATDC so that flame kernel formation and its growth can be detected albeit at atypical timing. Using the repetitive gating mode of the camera, three sets of 40 DIFs were captured at the required crank angles. The first set of DIFs was background images (BK) with both lasers on but both PFI and DI injectors off. The second set was motoring images (M) in which both lasers and PFI injector were on but the DI injector was

switched off. Finally the third set was the flame images (F) in which both lasers and both injectors were switched on. All three sets of images at each crank angle were captured following each other. To have the maximum spatial resolution no binning was applied during the image acquisition and image post processing. Figure 9a and 9b show the LIF full-field view of combustion chamber for the piston position at 35 CAD ATDC. The premix turbulent flame is shown after averaged background subtraction from a single flame image for laser excitation at 308 nm [$F(O)_{35\text{ CAD ATDC}}^{SIG} - BK(O)_{35\text{ CAD ATDC}}^{AVG}$] and 277 nm [$F(E)_{35\text{ CAD ATDC}}^{SIG} - BK(E)_{35\text{ CAD ATDC}}^{AVG}$]. The circular area has a diameter of 55 mm with resolution of 13.5 pixels/mm. To remove the effects of laser light attenuation across the imaging area, these images were divided by the background correct averaged motoring image for laser excitation at 308 nm [$M(O)_{35\text{ CAD ATDC}}^{AVG} - BK(O)_{35\text{ CAD ATDC}}^{AVG}$] and at 277nm [$M(E)_{35\text{ CAD ATDC}}^{AVG} - BK(E)_{35\text{ CAD ATDC}}^{AVG}$]. It should be noted that in order to remove the lasers' beam profile and further lessen the spatial intensity fluctuations of the excitation beams, additional techniques can be employed during imaging acquisition. In one of the most effective techniques, the output laser beam is split in several sections which are then overlapped in the focal plane of an imaging lens. This technique is usually based either on microlens arrays [50], random phase plates [51], or a combination of these [52]. It is shown that these beam homogenizers can also reduce temporal fluctuations in the laser beam profiles [53].

To obtain the temperature fields within and outside the flame area, the corrected single-line LIF image for laser excitation at 308 nm was divided by its 277 nm counterpart. Figure 9c shows the resultant image. While by applying a calibration curve on the final image, the in-cylinder charge temperature for the region outside the flame area can be calculated similar to the previous section; this image (R_{firing}) did not show any thermal stratification within the enflamed area neither presented a clear flame boundary. Consequently, in order to investigate the flame area, we clipped the pixel intensity level (for both excitation wavelengths) by setting a low and high clip values. The resultant images not only clearly showed the flame boundary but also distinguished the different zones of the flame. The logic behind this image processing step was that, we had two areas of the end-gas with high LIF signal level and enflamed area with a very low LIF signal level. The camera had a high dynamic range of 16 bit, which allowed us to capture both areas with a same gate width and gain values. But for the image processing, each area should be investigated separately as we cannot apply any single intensity scale that can represent both areas. While by clipping the intensity scale we could study single-line images, we could not obtain a satisfactory image for the ratio image in order to show the thermal stratification of the enflamed area. This was due to the fact that some image details were lost as the pixel intensity in certain areas fell outside the minimum and maximum cropped intensity scale.

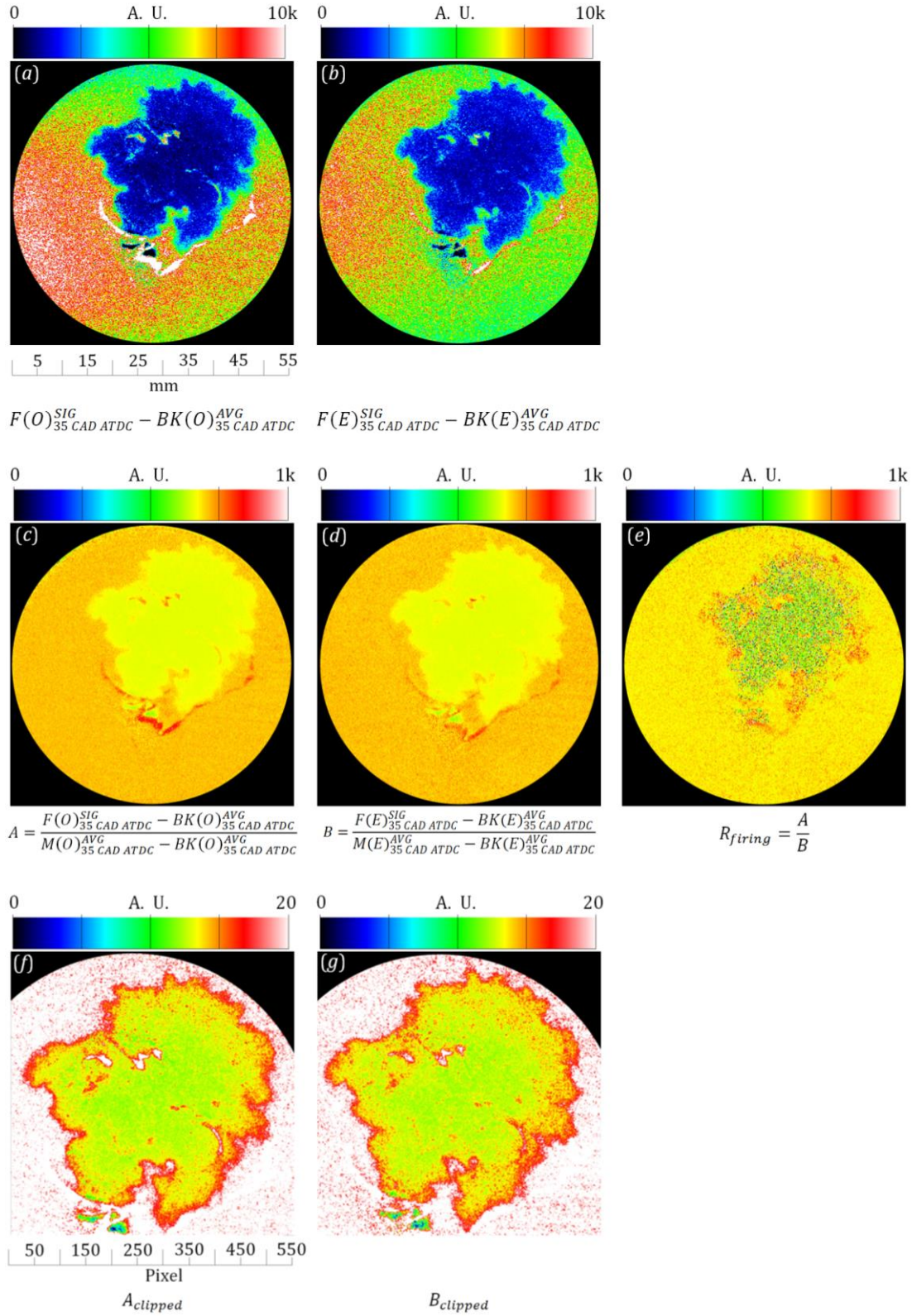


Fig. 9. PLIF full-field view images after background correction for (a) excitation at 308 nm, (b) excitation at 277 nm. (c), (d) after correction for the laser light attenuation. (e) The PLIF ratio image. (f), (g) Magnified enflamed area (550×550 pixel) after clipping the intensity scale.

In order to investigate thermal stratification of the enflamed area, an alternative image processing algorithm was utilized. The single flame image was subtracted from the averaged motoring image of the same crank angle for both excitation wavelengths at 308nm [$M(O)_{35\text{ CAD ATDC}}^{AVG} - F(O)_{35\text{ CAD ATDC}}^{SIG}$] and 277nm [$M(E)_{35\text{ CAD ATDC}}^{AVG} - F(E)_{35\text{ CAD ATDC}}^{SIG}$] to obtain the negative PLIF images. The resultant images are presented in Figure 10. In these specific images we have an asymmetrical flame growth towards the exhaust valve located on the upper right corner of the PLIF images. As the flame starts from the

spark plug and spreads out through the combustion chamber, the enflamed area at the vicinity of the spark plug represents the core of the flame where we expect to observe the combustion products while the area in contact with the end-gas represents reaction and preheat zones. The negative single-line PLIF images can clearly show the gradient of the dopant tracer concentration across the enflamed. We can further investigate flame structure if we focus on the upper right corner of these images. As the flame is relatively fresher in this section (compared to the area around the spark plug), it can present the actual flame structure more accurately. The end-gas region with a lower averaged pixel intensity is shown in dark blue. The relatively narrow light-blue/green band, with the width varying from ~ 0.1 mm to ~ 2 mm, enclosing the flame can be associated with the preheat zone where decomposition of the tracer starts. Then we have the reaction zone in orange/yellow colour which is almost twice thicker than the preheat zone. In this zone the flame temperature rises from the unburned charge temperature to the temperature of the combustion products in the luminous zone. And finally the product zone in red/white colour where most of the tracer has either decomposed or burnt. To determine the fluorescence intensity ratio and investigate thermal stratification across the flame, the single-line PLIF image at 308 nm [A'] was divided by its counterpart image at 277nm [B'] as shown in Eq.11.

$$R'_{firing} = \frac{M(O)_{35\text{ CAD ATDC}}^{AVG} - F(O)_{35\text{ CAD ATDC}}^{SIG}}{M(E)_{35\text{ CAD ATDC}}^{AVG} - F(E)_{35\text{ CAD ATDC}}^{SIG}} \quad (11)$$

By comparing Eq.11 with Eq.5 and Eq.6, the value of R'_{firing} can be shown to be a function of temperature and represent the thermal stratification of the enflamed region. Figure 10c shows the resultant ratio image. The engine spark plug was superimposed on this image and a number of ROIs with a size of 13×13 pixels ($\sim 0.93 \text{ mm}^2$) were assigned and the averaged fluorescence signal intensity ratio within each ROI was calculated. For a better visualization in Figure 10c, these ROIs are shown slightly bigger than their actual size. Figure 11 presents the measured averaged LIF signal intensity ratio of these ROIs. This value varies from 1.98 in the region 1 to 0.87 in the region 10, indicating a decrease of $\sim 55\%$ across the flame which can be translated to the temperature gradient. However for a quantitative measurements of the temperature fields, fluorescence signal from other combustion species should also be considered.

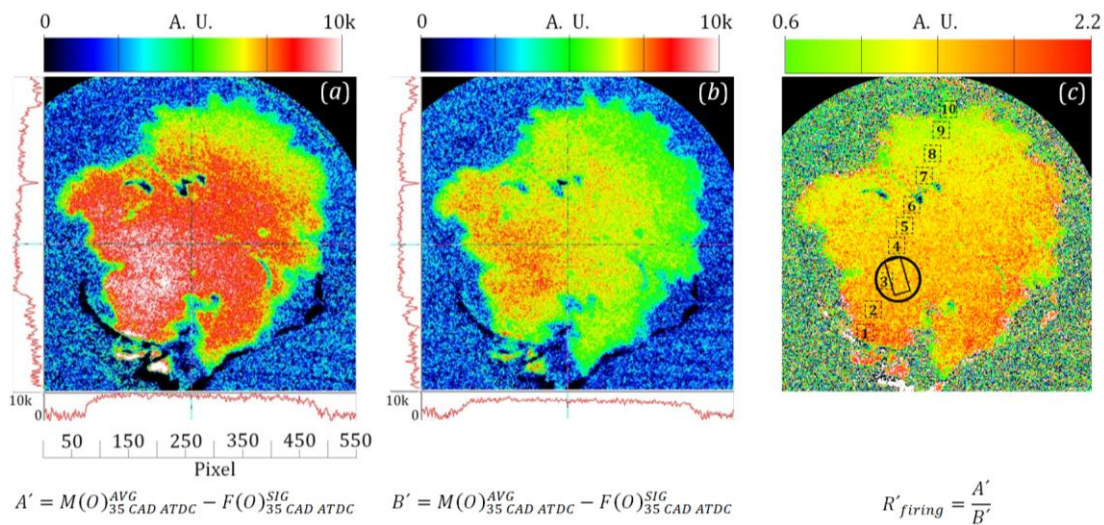


Fig. 10 Magnified enflamed area of the negative-PLIF images for (a) excitation at 308 nm, (b) excitation at 277 nm. (C) The negative-PLIF ratio image

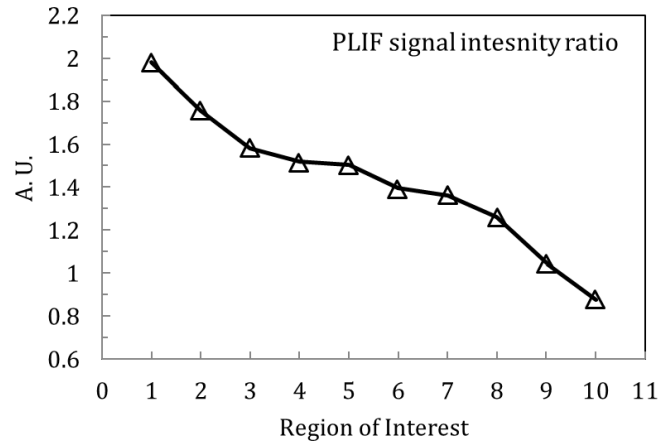


Fig. 11 Averaged negative-PLIF signal intensity ratio across the flame

5.2 Flame boundary detection

In direct photographic techniques usually a single threshold level is selected and applied to binarise the image. In this binary image the nonzero pixels are associated with the flame and zero pixels constitute the background and thus the flame structure is distinguished. However for the two-line PLIF images, tracing the exterior boundaries of the flame is not straight forward. This is due to the fact that unlike the direct photography that mostly captures the flame product zone, the two-line PLIF can record preheat, reaction and the product zones of the flame. As there is insufficient contrast between the flames' preheat zone and the end-gas, more advanced morphological techniques are required for the image processing. Thus a Matlab image processing code was written for the flame segmentation. This code calculated the gradient of the image from the end-gas region to the flame reaction zone to find a threshold value for the intensity image. For this purpose we used the 'edge' function and the 'Roberts' operator. The Roberts method was picked from the gradient-magnitude methods including Sobel and Prewitt. In these operators thresh is used to threshold the calculated gradient magnitude. They were compared with the Laplacian of Gaussian (Lap) which is a zero-crossing method and the Canny method. For the Lap, thresh is used as a threshold for the zero-crossings while the Canny method applies two thresholds to the gradient; a high threshold for low edge sensitivity and a low threshold for high edge sensitivity [54]. However none of these methods was capable of detecting our flame structure in a single step. The best result is obtained through an iterative process [55, 56]. To execute this algorithm; after initial 'edge' operation on the compliment of the intensity image, two linear horizontal and vertical structuring elements were created using 'strel' function and applied to dilate the end-gas region using 'imdilate' function. Then the 'imfill' function was applied to fill the holes and gaps in the resultant image. And the 'edge' function was employed for the second time to detect the flame boundary. After obtaining the flame boundary from both the two-line and the single-line PLIF images, a composite image was created as it is shown in Figure 12. In this fused image, the flame boundary obtained from single excitation wavelength at 308 nm (red boundary) was overlaid on the flame boundary obtained from the LIF ratio image (green boundary). The yellow area indicates the overlay of the two boundaries. By applying the code to other flame images, it was observed that the image processing algorithm can precisely calculate the flame front from both the single-line and the two-line PLIF images. No significant difference was observed between flame front calculated from the single-line and the two-line PLIF images. This was associated with the in-cylinder charge homogeneity and the tracer seeding mechanism. In these tests, using a port fuel injector, tracer was injected into heated intake port far from the cylinder head providing a very homogeneous mixture.

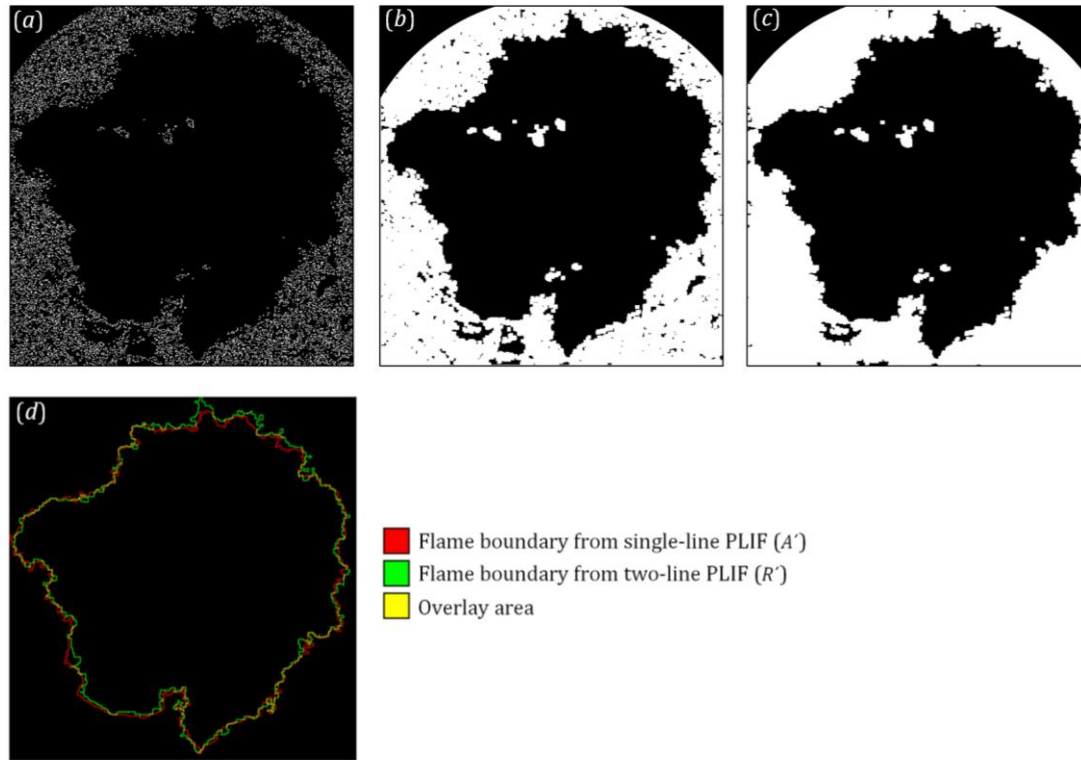


Fig. 12 Image processing steps for the flame boundary detection, (a) initial edge detection on the complement of the intensity image, (b) dilated image, (c) filled image, (d) flame boundary calculated from both single-line and two-line PLIF images.

4. Conclusion

The primary objective of this investigation was to extend the applications of the tracer-based two-line PLIF technique in combustion measurements. In particular, here we reported what we believe to be the first application of this diagnostic technique for investigation of turbulent flame boundary and structure. The PLIF setup was constructed for an optimized thermometry operation. The PLIF imaging was improved by utilizing variety of techniques for noise reduction prior and during image acquisition as well as applying a combination of post-processing techniques. Calibration curve of the fluorescence signal intensity ratio of the two laser beams and charge temperature was obtained through quasi in situ measurements, utilizing a specially designed constant volume chamber. Unlike the majority of previous studies whereby the two-line PLIF thermometry relies on a photophysical model of a dopant tracer, the calibration process enabled measurements of in-cylinder charge temperature independent of these models. To evaluate the PLIF thermometry results, average in-cylinder charge temperature during compression stroke of the control auto ignition operation was measured for both motoring and firing cycles and the PLIF values were compared with the temperature values calculated from in-cylinder pressure data where both technique showed a very good agreement. The two-line PLIF technique was employed to investigate the structure and the boundary of the turbulent flame during combustion process in an optical DISI engine. Although the single-line PLIF images can also be utilized for the flame boundary detection, but these images are dependent on the tracer or species concentration and thus can only be used for the premix flames in a homogenous charge prior to the ignition. On the other hand as the two-line PLIF images are independent of tracer and species concentration as well as the flame luminosity, they can be employed to study flame boundary and structure in non-homogeneously mixed systems. These conditions occur during stratified operation of DISI engines or e.g. during retarded direct injection timings and EGR recirculation. The test results indicated that the proposed technique has the ability to precisely detect the flame boundary and structure in the hostile environments of combusting media. The suggested technique can be used in calculating the flame stretch rates based on accurate flame boundary detection and reduce the disperse data reported on the engine flame behaviour. Future work will focus on further enhancing spatial and temporal resolutions of the PLIF technique. In addition, application of the beam homogenizers for removing the laser beams' profile will be considered. Development of more sophisticated image processing algorithms is another area aimed in future work. In particular, implementation of decision-based filters for detection and removal of the salt-pepper impulse noise are considered to be beneficial for improving the PLIF SNR and will be investigated.

Acknowledgments

The authors gratefully acknowledge financial support by the Engineering and Physical Sciences Research Council (EPSRC) in the frame of project "2-ACE"; reference EP/F058942/1.

References

- [1] H. Zhao, (ed), "Advanced Direct Injection Combustion Engine Technologies and Development," Vol.1: Gasoline and Gas Engines, Woodhead Publishing, 2010.
- [2] Y. Bianco, W. Cheng, J. Heywood, "The Effects of Initial Flame Kernel Conditions on Flame Development in SI Engine", SAE Technical Paper 912402, 1991, doi:10.4271/912402.
- [3] P. Aleiferis, A. Taylor, J. Whitelaw, K. Ishii, et al., "Cyclic Variations of Initial Flame Kernel Growth in a Honda VTEC-E Lean-Burn Spark-Ignition Engine", SAE Technical Paper 2000-01-1207, 2000, doi:10.4271/2000-01-1207.
- [4] R. M. Fristrom, A. A. Westenberg, "Flame Structure", McGraw-Hill, New York, 1965
- [4B] J. B. Heywood, "Internal Combustion Engine Fundamentals", McGraw-Hill Science Engineering, 1988.
- [5] B. Karlovitz, Jr., D.W. Denniston, D.H. Knapschaefer, F.E. Wells, "Studies on Turbulent flames. A. Flame Propagation Across velocity gradients B. turbulence Measurement in flames", Symposium (International) on Combustion, 1953, Vol.4 (1), pp.613-620, doi: 10.1016/S0082-0784(53)80082-2.
- [6] F. A. Williams, "A review of some theoretical considerations of turbulent flame structure". In: Paris: AGARD conference proceedings, vol. 164; 1975. III:1-25.
- [7] P. Witze, M. Hall, J. Wallace, "Fiber-Optic Instrumented Spark Plug for Measuring Early Flame Development in Spark Ignition Engines," SAE Technical Paper 881638, 1988, doi:10.4271/881638.
- [8] Y. Bianco, W. Cheng, J. Heywood, "The Effects of Initial Flame Kernel Conditions on Flame Development in SI Engine," SAE Technical Paper 912402, 1991, doi:10.4271/912402.
- [9] I. B. Zeldovich, A. S. Kompaneets, "Theory of Detonation", Academic Press Inc., New York, 1960.
- [10] W. Zeng, C. Idicheria, T. Fansler, and M. Drake, "Conditional Analysis of Enhanced Combustion Luminosity Imaging in a Spray-Guided Gasoline Engine with High Residual Fraction," SAE Technical Paper 2011-01-1281, 2011, doi:10.4271/2011-01-1281.
- [11] M. Ahmadi, M. Saffar Avval, T. Yousefi, M. Goharkhah, B. Nasr, M. Ashjaee, "Temperature measurement of a premixed radially symmetric methane flame jet using the Mach-Zehnder Interferometry", J of Optics and Lasers in Engineering, Volume 49, Issue 7, July 2011, 859-865, 10.1016/j.optlaseng.2011.02.020
- [12] A. Murty Kanury, "Introduction to Combustion Phenomena", Gordon and Breach Science Publishers Inc., New York, 1975.
- [13] I. Glassman, "Combustion", Academic Press Inc., London, 1977.
- [14] T. Baritaud, R. Green, "A 2-D Flame Visualisation Technique Applied to the I.C. Engine," SAE Technical Paper 860025, 1986, doi:10.4271/860025.
- [15] G. Ziegler, A. Zettlitz, P. Meinhardt, R. Herweg, et al., "Cycle-Resolved Two-Dimensional Flame Visualization in a Spark-Ignition Engine," SAE Technical Paper 881634, 1988, doi:10.4271/881634.
- [16] R. Hicks, M. Lawes, C. Sheppard, B. Whitaker, "Multiple Laser Sheet Imaging Investigation of Turbulent Flame Structure in a Spark Ignition Engine," SAE Technical Paper 941992, 1994, doi:10.4271/941992.
- [17] M. Aldén, H. Edner, G. Holmstedt, S. Svanberg, and T. Högberg, "Single-pulse laser-induced OH fluorescence in an atmospheric flame, spatially resolved with a diode array detector", Applied Optics, Vol. 21, Issue 7, pp. 1236-1240 (1982) doi:10.1364/AO.21.001236.
- [18] G. Kychakoff, R. D. Howe, R. K. Hanson, J. C. McDaniel, "Quantitative visualization of combustion species in a plane", Applied Optics, Vol. 21, Issue 18, 3225-3227 (1982), doi:10.1364/AO.21.003225.
- [19] M. J. Dyer, D. R. Crosley, "Two-dimensional imaging of OH laser-induced fluorescence in a flame", Optics Letters, Vol. 7, Issue 8, 382-384 (1982), doi:10.1364/OL.7.000382.
- [20] G. Kychakoff, K. Knapp, R. D. Howe, R. K. Hanson, "Flow visualisation in combustion gases using nitric oxide fluorescence", AIAA J. 22,153, 1984.
- [21] M. P. Lee, P. H. Paul, R. K. Hanson, "Laser-fluorescence imaging of O₂ in combustion flows using an ArF laser", Optics Letters, Vol. 11, Issue 1, pp. 7-9 (1986), doi:10.1364/OL.11.000007.
- [22] D. Bradley, C. G. W. Sheppard, R. Woolley, D. Greenhalgh, R. D. Lockett, "The development and structure of flame instabilities and cellularity at low Markstein numbers in explosions", Combustion and Flame, 122:195-209 (2000), doi: 10.1016/S0010-2180(00)00113-9.
- [23] T. Strand, D. Rothamer, J. Ghandhi, "Flame Structure Visualization of Stratified Combustion in a DISI Engine via PLIF," SAE Technical Paper 2001-01-3649, 2001, doi:10.4271/2001-01-3649.
- [24] A. Arnold, H. Becker, R. Suntz, P. Monkhouse, J. Wolfrum, R. Maly and W. Pfister "Flame front imaging in an internal-combustion engine simulator by laser-induced fluorescence of acetaldehyde", OPTICS LETTERS, Vol. 15, No. 15
- [25] F. Zhao, M. Lai, D. Harrington, "A Review of Mixture Preparation and Combustion Control Strategies for Spark-Ignited Direct-Injection Gasoline Engines," SAE Technical Paper 970627, 1997, doi:10.4271/970627.
- [26] P. Price, P. Twiney, B. Stone, R. Kar, et al., "Particulate and Hydrocarbon Emissions from a Spray Guided Direct Injection Spark Ignition Engine with Oxygenate Fuel Blends," SAE Technical Paper 2007-01-0472, 2007, doi:10.4271/2007-01-0472.
- [27] A. C. Eckbreth, "Laser Diagnostics for Combustion Temperature and Species", 2nd edn., Gordon and Breach, New York, 1996.
- [28] H. Zhao, N. Ladommatos, "Engine Combustion Instrumentation and Diagnostics". Warrendale, PA: Society of Automotive Engineers, 2001.
- [29] H. Shengteng, W. Peiyong, W. P. Robert, "A structural study of premixed tubular flames", J of Proceedings of the Combustion Institute, Volume 32, Issue 1, 2009, Pages 1133-1140, 10.1016/j.proci.2008.06.183.

- [30] H. Shengteng, W. P. Robert, "Structural study of non-premixed tubular hydrocarbon flames", *J of Combustion and Flame*, 156 (2009) 51–61, 10.1016/j.combustflame.2008.07.017.
- [31] A. Leipertz, G. Kowalewski, and S., Kampmann, "Measurement of gas temperature and temperature structures in premixed flames by using laser Rayleigh techniques," in *Temperature: Its Measurement and Control in Science and Industry*, Am. Institute of Physics, New York, 1992, pp. 685-690.
- [32] R. A. Patton, K. N. Gabet, N. Jiang, W. R. Lempert, J. A. Sutton, "Multi-kHz temperature imaging in turbulent non-premixed flames using planar Rayleigh scattering", *J of Applied Physics B*, Volume 108, Issue 2, pp 377-392, 10.1007/s00340-012-4880-5.
- [33] K. N. Gabet, N. Jiang, W. R. Lempert, J. A. Sutton, "Demonstration of high-speed 1D Raman scattering line imaging", *J of Appl. Phys. B* 101, 1-5, 10.1007/s00340-010-4208-2.
- [34] N. M. Laurendeau, "Temperature Measurements by Light Scattering Methods", in N., Chigier, (ed.) "Combustion Measurements", Hemisphere Pub. Corp., Washington, DC. 1991.
- [35] T. Baritaud, T. Heinze, "Gasoline Distribution Measurements with PLIF in a SI Engine," SAE Technical Paper 922355, 1992, doi:10.4271/922355.
- [36] D. Hansen, E. Lee, "Radiative and nonradiative transitions in the first excited singlet state of symmetrical methyl-substituted acetones", *J Chem Phys* 62:183–189, 1975.
- [37] J. B. Gandhi, P. G. Felton, "On the fluorescence behavior of ketones at high temperatures," *Exp. Fluids*, Vol. 21, Issue 2, pp 143-144, 1996, doi:10.1007/BF00193918.
- [38] F. Grossmann, P. Monkhouse, M. Ridder, V. Sick, J. Wolfrum, "Temperature and Pressure Dependences of the Laser-Induced Fluorescence of Gas-Phase Acetone and 3-Pentanone," *Applied Physics B* 62 (3): 249-253, 1996, doi:10.1007/BF01080952.
- [39] F. Ossler, M. Alden, "Measurements of picosecond laser induced fluorescence from gas-phase 3-pentanone and acetone: Implications to combustion diagnostics", *Appl. Phys. B* 64, 493–502, 1997.
- [40] F. Grossmann, P. Monkhouse, M. Ridder, V. Sick, J. Wolfrum, "Temperature and pressure dependences of the laser-induced fluorescence of gas-phase acetone and 3-pentanone", *Applied Physics B*, Volume 62, Issue 3, 249-253, 1996, doi: 10.1007/BF01080952.
- [41] Einecke, S., Schulz, C., Sick, V., Dreizler, A. et al., "Two-Dimensional Temperature Measurements in an SI Engine Using Two-Line Tracer LIF," SAE Technical Paper 982468, 1998, doi:10.4271/982468.
- [42] Rothamer, D., Snyder, J., Hanson, R., and Steeper, R., "Two-Wavelength PLIF Diagnostic for Temperature and Composition," *SAE Int. J. Fuels Lubr.* 1(1):520-533, 2009, doi:10.4271/2008-01-1067.
- [43] Snyder, J., Dronniou, N., Dec, J., and Hanson, R., "PLIF Measurements of Thermal Stratification in an HCCI Engine under Fired Operation," *SAE Int. J. Engines* 4(1):1669-1688, 2011, doi:10.4271/2011-01-1291.
- [44] M. Anbari Attar, M. R. Herfatmanesh, H. Zhao, A. Cairns, "Experimental Investigation of Direct Injection Charge Cooling in Optical GDI Engine Using Tracer-based PLIF Technique", *Journal of Experimental Thermal and Fluid Science*, 10.1016/j.expthermflusci.2014.07.020.
- [45] L. S. Yuen, J. E. Peters, and R. P. Lucht, "Pressure dependence of laser-induced fluorescence from acetone," *Appl. Opt.* 36, 3271–3277 (1997).
- [46] M. C. Thurber, F. Grisch, B. J. Kirby, M. Votsmeier, and R. K. Hanson, "Measurements and modeling of acetone laser induced fluorescence with implications for temperature imaging diagnostics," *Appl. Opt.* 37, 4963–4978, 1998.
- [47] A. Braeuer, F. Beyrau, and A. Leipertz, "Laser induced fluorescence of ketones at elevated temperatures for pressures up to 20 bars by using a 248 nm excitation laser wavelength: experiments and model improvements", *Applied Optics*, 45(20):4982–4989, 2006.
- [48] W. R. Ware and S. K. Lee, "Luminescent properties of hexafluoroacetone. II. Fluorescence quenching by oxygen, nitric oxide and unsaturated hydrocarbons," *J. Chemical Physics*, 49, 217–220, 1968.
- [49] Iida, N., Yamasaki, Y., Sato, S., Kumano, K. et al., "Study on Auto-Ignition and Combustion Mechanism of HCCI Engine," SAE Technical Paper 2004-32-0095, 2004, doi:10.4271/2004-32-0095.
- [50] F. X. Wagner, M. Scaggs, A. Koch, H. Endert, H. M. Christen, L. A. Knauss, K. S. Harshavardhan, S. M. Green, "Epitaxial HTS thin films grown by PLD with a beam homogenizer", *Applied Surface Science*, Volumes 127–129, May 1998, Pages 477–480, doi:10.1016/S0169-4332(97)00677-6.
- [51] C. L. S. Lewis, I. Weaver, L. A. Doyle, G. W. Martin, T. Morrow, D. A. Pepler, C. N. Danson, *Review of Scientific Instruments* Vol. 70, Issue 4, 2116-2121 (1999).
- [52] C. Kopp, L. Ravel, and P. Meyrueis, "Efficient beamshaper homogenizer design combining diffractive optical elements, microlens array and random phase plate," *J. Opt. A, Pure Appl. Opt.* 1(3), 398–403, 1999, doi:10.1088/1464-4258/1/3/310.
- [53] S. Pfadler, F. Beyrau, M. Löffler, and A. Leipertz, "Application of a beam homogenizer to planar laser diagnostics," *Optics Express*, Vol. 14, Issue 22, pp. 10171-10180, 2006, doi: 10.1364/OE.14.010171.
- [54] J. Canny, "A Computational Approach to Edge Detection", *IEEE Transactions on Pattern Analysis and Machine Intelligence*, Vol. PAMI-8, No. 6, 1986, pp. 679-698.
- [55] R. C. Gonzalez, R. E. Woods, S. L. Eddins, "Digital Image Processing Using MATLAB", New Jersey, Pearson Prentice Hall, 2004.
- [56] R. J. Parker, "Algorithms for Image Processing and Computer Vision", New York, John Wiley & Sons, Inc., 1997.